Thermal-integration in Photoelectrochemistry for Fuel and Heat Co-Generation

(Supplementary Information)

Evan F Johnson, Sophia Haussener
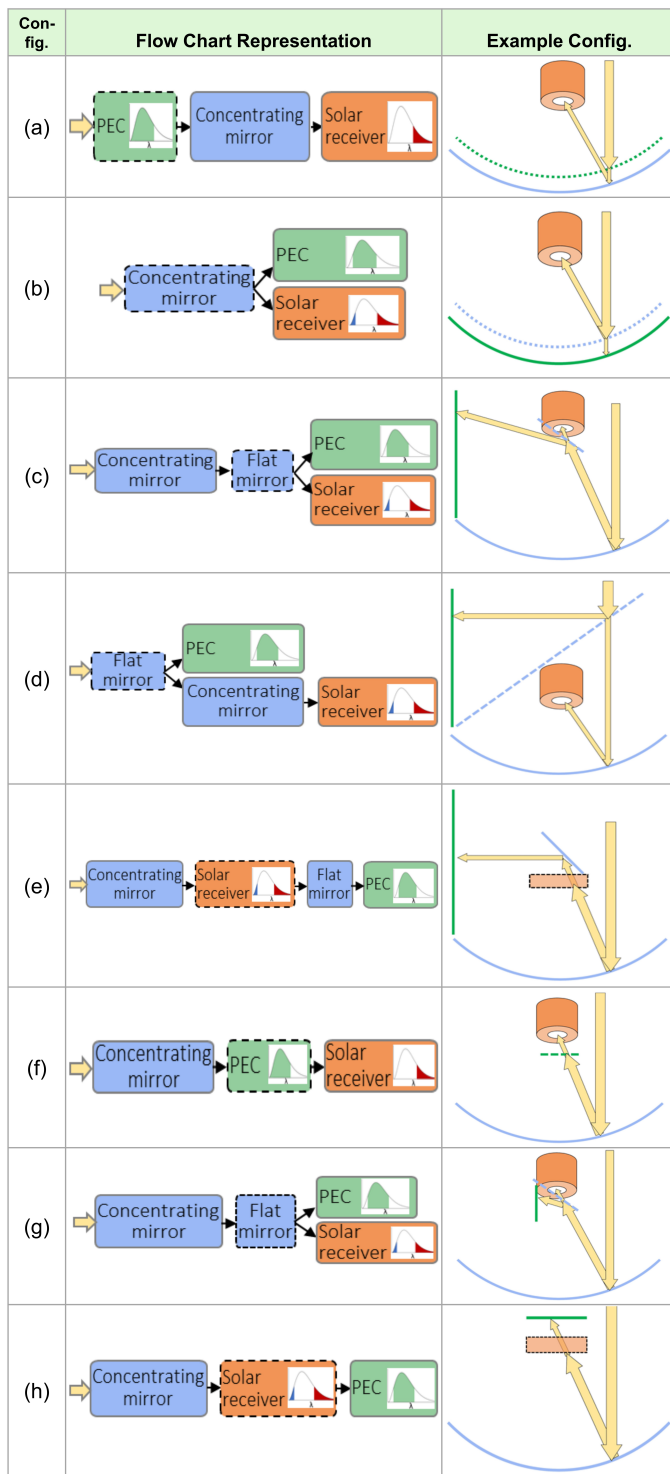
Config.	Flow Chart Representation	Example Config.
(a)	PEC → Concentrating mirror → Solar receiver	
(b)	Concentrating mirror → {PEC, Solar receiver}	
(c)	Concentrating mirror → Flat mirror → {PEC, Solar receiver}	
(d)	Flat mirror → {PEC, Concentrating mirror → Solar receiver}	
(e)	Concentrating mirror → Solar receiver → Flat mirror → PEC	
(f)	Concentrating mirror → PEC → Solar receiver	
(g)	Concentrating mirror → Flat mirror → {PEC, Solar receiver}	
(h)	Concentrating mirror → Solar receiver → PEC	

Fig. S1 Vapor and liquid PEC configurations employing solar concentration and spectrum splitting for heat collection. In diagrams, PEC is green, mirrors are blue, and receiver is orange, with the spectrally selective component shown with a dashed line.

S1 Beam Splitting Configurations

Numerous possible beam splitting configurations for parabolic dish systems are shown in Fig. S1, with the solar energy entering on the left (yellow arrow) and ending at the PEC and the solar receiver. The icon of the spectrum shows the absorbed wavelengths for the PEC and solar receiver, as some designs split only the low-energy photons for heating, while others can also use high-energy photons. The "Example" column shows how the configuration could be constructed, though there may be numerous ways to build the configuration shown by each block diagram.

Configurations (a)-(e) have no concentration on the PEC, which is required for vapor-fed PEC devices, as they can sustain very little concentration before overheating. As discussed in Section 2.2, a slight concentration (<10 suns) may be possible, but in the configurations presented here, no concentration on the PEC is assumed on the vapor-fed designs. Liquid based designs have no such limit, so all configurations are viable for liquid.

In configuration (a), the PEC itself is spectrally selective, where all photons with energy less than the lower band gap are transmitted through the PEC. This would require a PEC to be constructed with transparent encapsulation. To the knowledge of the authors, a transparent-encapsulated PEC has not been constructed to date, yet no fundamental barriers to its construction are foreseen. In this configuration, photons would actually pass through the PEC before and after being reflected by the parabolic mirror. To minimize materials, the mirror surface and the PEC may actually be constructed together, integrated into the same support structure. Since all photons above the lower band gap are absorbed by the PEC, it is only possible with this configuration to let the low-energy photons pass. However, a significant benefit of this design is that the PEC can use diffuse radiation, whereas designs with a concentrator before the PEC (designs (c)-(h)) can only use beam radiation.

Configurations (b)-(d) each use a spectrally splitting (e.g. dichroic) mirror. Configuration (b) shows a parabolic shaped dichroic mirror with the surface area matching the PEC. Current dichroic mirrors are small, high-value optics components, so this design is unfeasible until large-format, spectrally selective optics components are available. Configuration (c) uses a typical parabolic concentrator and a small selective mirror, which may decrease cost, but the acceptance angles of the selective mirror may cause optical losses, and active cooling of the mirror may be required. The photons are split near the focus, and photons destined for the PEC spread back out to the original concentration. Configuration (d) also requires a large-format selective mirror. Since these configurations rely on a selective mirror specifically designed for the purpose, they may employ both a low and high energy cutoff, which gives more flexibility to optimize heat collection.

Configuration (e) splits the spectrum with a selective absorber. Photons not absorbed by the receiver are directed to the PEC via a flat mirror, returning to a concentration of 1, as required for the vapor-fed designs. The flat mirror is required, as placing the PEC directly above the receiver would shade the concentrator. With this configuration, the receiver needs to have an opening on two sides (one inlet and one outlet for light), so that the cavity-type solar receiver shown for the other designs cannot be used. Cavity receivers are used to limit emissive losses at high temperatures, but the selective absorber may be viable for low temperature heat collection (e.g. <150°C).

Configurations (f)-(g) use concentration on the PEC, so these are only applicable for liquid-fed PEC devices. In configuration (f), the PEC selectively absorbs photons, similar to (a), requiring the PEC to be built with transparent encapsulation. Configuration (g) uses a selective mirror, similar to (c), but concentrated light strikes the PEC close to the selective mirror. Configuration (h) uses a selective absorber, which appears to be a simple design for low temperatures but may not be applicable for high temperature applications.

S2 PEC Heat Balance

The equations constituting the PEC heat balance are given in Equations S1 to S7, corresponding to Figure S2. The incident radiation (q''_{rad}) is the combination of direct radiation ($q''_{beam,inc}$) multiplied by the concentration factor (C), and in the case of non-concentrating systems the diffuse component is also included ($q''_{diff,inc}$). The radiation reaching the PEC surface is reduced by the optical efficiency ($\eta_{opt,PEC}$) due to losses from the glass (shown as q''_{glass}) and concentrating mirrors (not shown). In this analysis, the losses from the PEC surface include reflection (q''_{refl}), radiative emission from the top (q''_{emiss}), and convection to the air stream (q''_{conv}). The back side is assumed to be insulated as it is expected that the PEC encapsulation will have a significant resistance to heat flow. Radiative energy converted to chemical energy (q''_{H2}) acts as an energy sink in the heat balance, which depends on the solar-to-hydrogen efficiency (η_{STH}). The convection coefficient to the air stream is based on the hydraulic diameter for parallel plates ($2 \cdot t_{gap}$) and a Nusselt number for fully developed flow with uniform heat flux, i.e. 4.86.

For the analysis on the maximum temperature at various solar concentrations (Section 2.2), a solar-to-hydrogen efficiency (η_{STH}) of 10% is assumed, with an incident beam radiation of 1000 W/m^2. The optical efficiency ($\eta_{opt,PEC}$) is composed of one mirror and one glass with individual efficiencies of 0.94 and 0.92, respectively.

In the analysis on PEC system configurations (Section 4), the solar-to-hydrogen efficiency is not assumed, and instead it is calculated using the intersection of the PV-EC curves. The on-sun area is 4.9 m^2 in each case, corresponding to a 2.5 m diameter dish. For cases with concentrated radiation on the PEC (Type 3 and 4) the PEC area is set equal to the solar receiver aperture, 0.005 m^2, corresponding to a diameter of 8 cm.

$$q''_{rad} = q''_{H2} + q''_{refl} + q''_{emiss} + q''_{conv} \tag{S1}$$

$$q''_{rad} = (Cq''_{beam,inc} + q''_{diff,inc})\eta_{opt,PEC} \tag{S2}$$

$$q''_{H2} = \eta_{S-H}q''_{rad} \tag{S3}$$

$$q''_{refl} = \rho q''_{rad} \tag{S4}$$

$$q''_{emiss} = \sigma\varepsilon(T_{PEC}^4 - T_{inf}^4) \tag{S5}$$

$$q''_{conv} = h_f\left(T_{PEC} - \frac{T_{in} + T_{out}}{2}\right) \tag{S6}$$

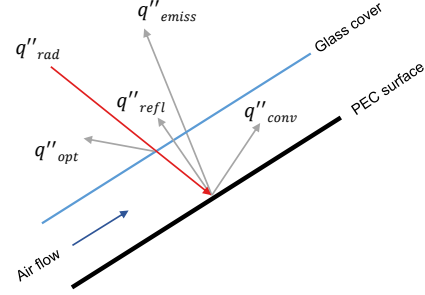$$q''_{conv} = \frac{\dot{m}_{air}C_p}{A_{PEC}}(T_{out} - T_{in}) \tag{S7}$$

Fig. S2 Heat balance of PEC used to find steady state surface temperature under various radiation and concentration conditions.

S3 Estimation of i_{lim} from experimental data

In the present work, i_{lim} is estimated from experimental data by Kumari et al.[5] Their data set gives vapor-fed electrolyzer curves at various relative humidities and flow rates from seawater-humidified air over Pt/C electrodes, from which it appears that i_{lim} increases linearly with both of these parameters. The limiting current is estimated from the experimental data and plotted against the flow rate and relative humidity (Figure S3), and linear scaling factors are found to estimate i_{lim} for any relative humidity and flow rate within the experimental range. These factors are combined to form Eq. S8, where RH is the relative humidity (in percentage), Q_{exp} is the experimental flow rate (20 SCCM), and Q is the flow rate at which the i_{lim} is desired. Finally, to relate a larger PEC device to the experimental conditions, the flow rate from the larger PEC is first scaled by a ratio of the cross sectional areas ($A_{experiment}/A$) to align the mass flux of vapor between the two designs. Experimental data is only available at room temperature, so temperature dependence of the EC is neglected. Thus, i_{lim} is estimated for an arbitrary relative humidity and flow rate, and it is then used in Eq. 7 to fully define the electrolyzer curve for the desired conditions. In Figure 5, the experimental curve with RH=80% and Q=20 SCCM is taken as the base case, and the curve is scaled according to $i_{lim}/i_{lim,base-case}$ to visualize the experimental curve for various flow rates. The modeled vapor curves are shown in dashed lines, with fitted constants c_1=-0.6105, c_2=0.09659, and c_3=0.0009717. A nonzero current is shown by the experimental curves below 1.23 V, but this is excluded from curve fitting as it cannot be attributed to the hydrogen evolution reaction.
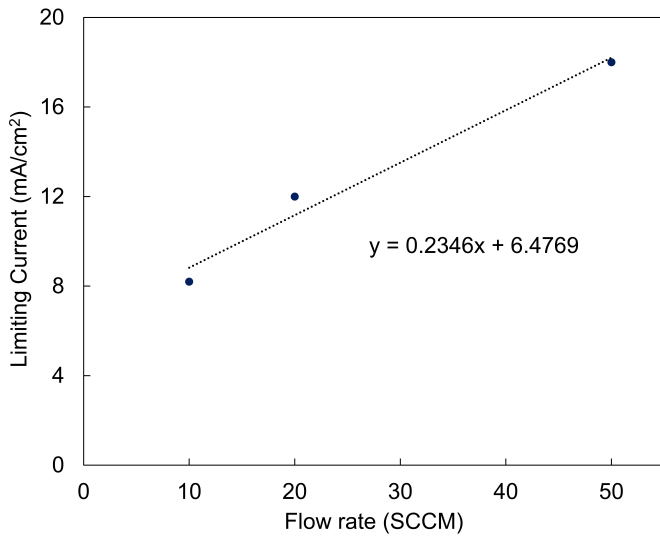
$$i_{lim} = 1.725 + 0.1432RH + 0.2346(Q - Q_{exp}) \tag{S8}$$

S4 Tracking Schemes

First, a south-facing, fixed-tilt system is modeled with tilt angle $\beta = 45°$. The convention for azimuth angles (Θ) is adopted with north as $0°$, so $\Theta_{PEC}=180°$ for the fixed-tilt system. The second scheme is single-axis tracking with a north-south axis, which is
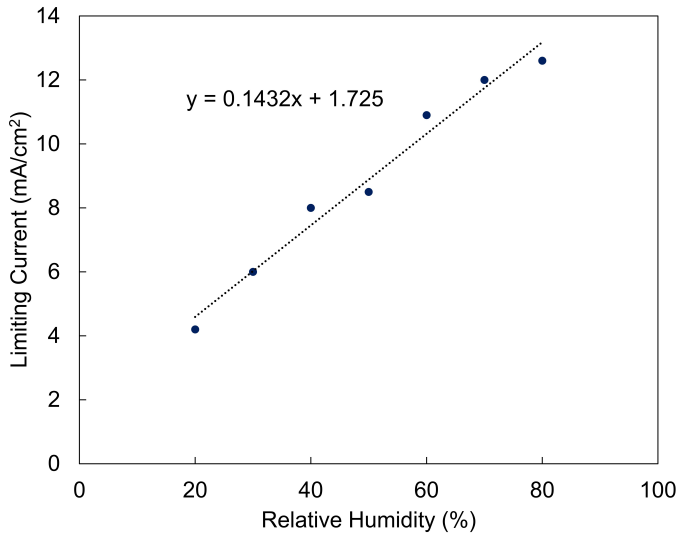
(a)

(b)

Fig. S3 Limiting current as a function of (a) relative humidity with flow rate of 20 SCCM, and (b) flow rate with RH=80%.

common for utility-scale PV systems. The inclination and azimuth angles for single-axis tracking are shown in Eq. S9, where β is the tilt angle of the PEC, α_{sun} is the elevation angle of the sun, and Θ_{PEC} and Θ_{sun} are the azimuth angles. With this equation, Θ_{PEC} is set to 90° for $\Theta_{sun}<180°$ (morning hours) and 270° otherwise (afternoon hours). The equation is adapted from Braun and Mitchell[2], after adjusting for the 0°=north convention and using the sun elevation angle instead of the zenith angle. For two-axis tracking, the PEC receives the full DNI at each hour of the day by setting the $\Theta_{PEC} = \Theta sun$ and $\beta = 90° - \alpha_{sun}$.

$$\tan(\beta_{1-axis}) = \tan(90° - \alpha_{sun})\cos(\Theta_{PEC} - \Theta_{sun}) \quad (S9)$$

For each tracking system, the beam radiation incident upon the PEC surface ($q''_{beam,inc}$) is calculated with Eq. S10 by accounting

for cosine losses, using the equations of Braun,[2] with the zenith angle defined as $90° - \alpha_{sun}$. In addition, diffuse radiation incident to the PEC surface ($q''_{diff,inc}$) is calculated with Eq. S11[4] from the horizontal diffuse value ($q''_{diff,h}$). The two incident radiation values are added to find the total incident radiative flux on the PEC surface at each hour of the day. The DNI and horizontal diffuse radiation values are taken from the TMY4 data set.[10]

$$q''_{beam,inc} = DNI\,[\cos(90° - \alpha_{sun})\cos(\beta)+$$
$$\sin(90° - \alpha_{sun})\sin(\beta)\cos(\Theta_{sun} - \Theta_{PEC})] \quad (S10)$$

$$q''_{diff,inc} = q''_{diff,h}\left[\frac{1+\cos(\beta)}{2}\right] \quad (S11)$$

S5 Hourly Solar Profile

The hourly solar radiation profiles used in this work are shown in Fig. S4, for (a) April 16th in Paris, France, and (b) March 17th in Daggett, California, USA. Dashed lines indicate DNI and horizontal diffuse radiation given by the TMY data set, and dashed lines show the calculated incident radiation on a surface with various tracking options.

S6 Extra Results

The PV and EC curves are shown for the base case band gaps (1.2 and 1.788 eV) for each system configuration in Fig. S5, corresponding to the analysis in Section 4.1.

S7 Diode Equation for Non-Ideal Photoabsorbers

The non-ideal photoabsorption curve is modeled with Eqs. S12 and S13, where i_{SC} and V_{OC} are the short circuit current and open circuit voltages, which are taken from the Shockley-Queisser equations. The R_{sh} and R_{ser} are the shunt and series resistances, 0.006 and 0.004 Ω, respectively, chosen to achieve a roughly 5% solar to hydrogen efficiency.

$$i = i_{sc} - i_d \exp\left(\frac{V + iR_{ser}}{V_{th}}\right) - \frac{V + iR_{ser}}{R_{sh}} \quad (S12)$$

$$i_d = i_{sc} \exp\left(-\frac{V_{oc}}{V_{th}}\right) \quad (S13)$$

S8 Parameters

Parameters used in exergy calculations are given in Table S1.

S9 Solar Air Receiver

Air receivers can either absorb radiation volumetrically such as in ceramic foams[7], or on a conductive surface, transferring heat to the fluid flowing behind it. Volumetric receivers must be either covered with a quartz window for positive pressure pumping, or they are open to the atmosphere but require vacuum pumping[7] both technical hurdles. Therefore, a surface absorbing receiver studied by Hischier[3] and Pozivil[8] is chosen. Rays enter the cavity, strike a ceramic surface, and heat is transferred to the air flowing behind the surface, which is enhanced via a conductive ceramic foam. The detailed numerical model by[3] uses computational fluid dynamics. In the present work, a similar receiver
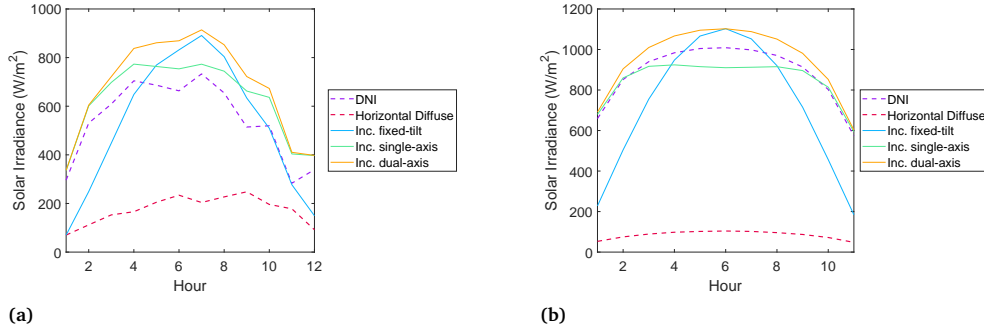
Fig. S4 Direct normal and horizontal diffuse irradiance (dashed lines) at each hour of the day, and calculated irradiance incident upon the PEC surface with each of the three tracking methods (solid lines), for (a) Paris, France, and (b) Daggett, California, USA.

Table S1 Properties used in exergy calculations at pressure of 101.325 kPa.

Property	Temperature (°C)	Value	Units	Source
h_{air}	20	293.56	kJkg^{-1}	6
h_{air}	65	338.92	kJkg^{-1}	6
h_{air}	500	793.3	kJkg^{-1}	6
$h_{H_2O,liq}$	20	84.01	kJkg^{-1}	6
$h_{H_2O,liq}$	65	272.14	kJkg^{-1}	6
s_{air}	20	6.848	kJ kg^{-1}	6
s_{air}	65	6.992	kJ kg^{-1}K^{-1}	6
s_{air}	500	7.852	kJ kg^{-1}K^{-1}	6
$s_{H_2O,liq}$	20	0.2965	kJkg^{-1}K^{-1}	6
$s_{H_2O,liq}$	65	0.8935	kJkg^{-1}K^{-1}	6
$b_{H_2O,liq}$	25	0.9	kJmol^{-1}	9
$b_{H_2O,vap}$	25	9.5	kJmol^{-1}	9
b_{H_2}	25	236.09	kJmol^{-1}	9

design is adopted, but the analysis is carried out using a simplified quasi-2D model, as the goal is to predict trends in overall system behavior for a wide array of operating conditions.

A cross-section of the cylindrically shaped receiver model is shown in Figure S7(a). Air enters the flow chamber (gold color) near the aperture at 100°C and is heated before leaving out the back of the receiver. To fulfill the role of the conductive ceramic foam in [3] the flow chamber modeled has a bank of cylinders perpendicular to the absorbing surface, with a center-to-center spacing of 8 mm and a diameter of 1 mm. Under the conditions modeled, concentrated radiation enters the aperture according to Eq. 11, where the parabolic dish area A_{inc} is 4.91 m^2 (for a diameter of 2.5 m), DNI is the direct normal irradiance, $\eta_{opt,rcv}$ is the optical loss due to mirror (reflectivity of 0.94) and glass sheet (transmissivity of 0.92), and the fraction of spilled radiation (η_{spill}) is 0.85. The filtering transmissivity (τ) is the fraction of radiation transmitted to the receiver after beam splitting, either by absorption by the semitransparent PEC or by a spectrally splitting mirror. The useful heat convected to the air stream is calculated with an empirical relation for heat transfer to a bank of cylinders with a uniform surface temperature, classified by the average Nusselt given in Eq. S14. [1] In this analysis, the absorber surface and cylinders are assumed to be at a uniform temperature, as the distance

is small and conductive material is assumed. The cavity has an interior diameter of 11 cm, an aperture diameter of 8 cm, the flow channel has a thickness of 1 cm, and the insulation has a thickness of 10 cm. Heat losses through the aperture are due to reflection, radiative emission, and convection from the aperture. [1] Additional heat is lost via conduction through the insulation and subsequent convection and radiation to the surroundings. The incident radiation (Eq. 11) is balanced with these loss modes to find the mass flow rate of air, the air outlet temperature, the absorber surface temperature, the overall heat gain, and the thermal efficiency.

$$\overline{Nu}_D = C_1 Re_{D,\max}^m \Pr^{0.36} \left(\frac{Pr}{Pr_s} \right)^{1/4} \quad (S14)$$

Before implementing the solar receiver model into the larger model to analyze specific beam-splitting configurations, it is run in isolation for a range of temperatures and filtering values to predict the performance under various conditions. Figure S7(b) shows results in terms of heat gain to the air stream and the thermal efficiency, defined as the fraction of energy entering the aperture which is delivered to the air stream ($\eta_{theraml} = \frac{\dot{m}c_p \cdot (T_{exit} - T_{in})}{q''_{rad}}$). Transmission values were varied from 0.10 up to 1, and various outlet temperatures are achieved by modifying the mass flow rate of air. With $\tau=1$ (blue), the solar receiver has no filtering, and efficiency is in the same range and shows the same downward trend as predicted by the higher fidelity models of Hischier[3] and Pozivil.[8] The lines for different τ values show that the thermal efficiency is reduced as τ is reduced, which is due to thermal losses remaining roughly constant for a certain outlet temperature, while the energy entering the aperture is reduced. The trend has implications for supplying heated air to industrial processes at high temperatures. For example, to supply air at 600°C, if 70% of the spectrum is diverted to the PEC ($\tau=0.30$), a thermal efficiency of 59% is expected, which may be high enough to supply useful heat to a process. Higher temperatures and lower τ values both lead to lower thermal efficiencies, especially when approaching 1000°C and for filtering below $\tau=0.20$. In addition to the low efficiency, low τ values lead to low heat gain, as the solar receiver is exposed to very low intensity light. In the moderate ranges of τ, between 0.2 and 0.6, there may be regions where the overall value of the hydrogen and collected heat is beneficial
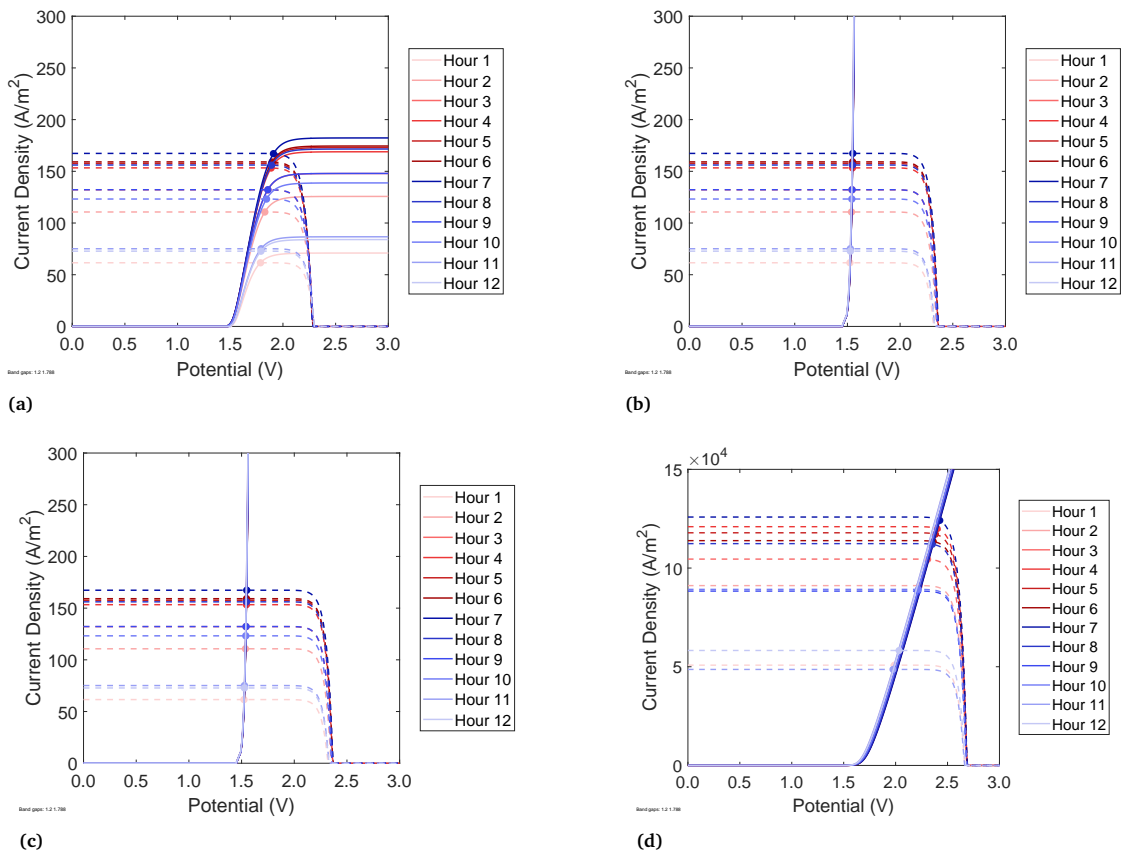
(a)

(b)

(c)

(d)

Fig. S5 Photoabsorber and electrochemical curves for system types (a)Type1-vap, (b)Type1-liq, (c) Type2-liq, and (d) Type4-liq.

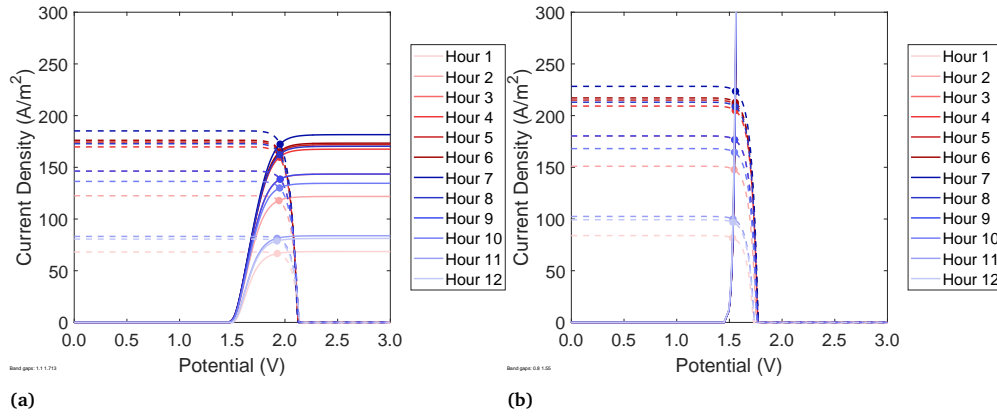and economical for certain industrial processes.

Fig. S6 PV and EC curves for Type1 system at bad gaps of peak H_2 output, (a) vapor reactant at E_g values of 1.1 and 1.713 eV, and (b) liquid reactant with 0.8 and 1.55 eV.
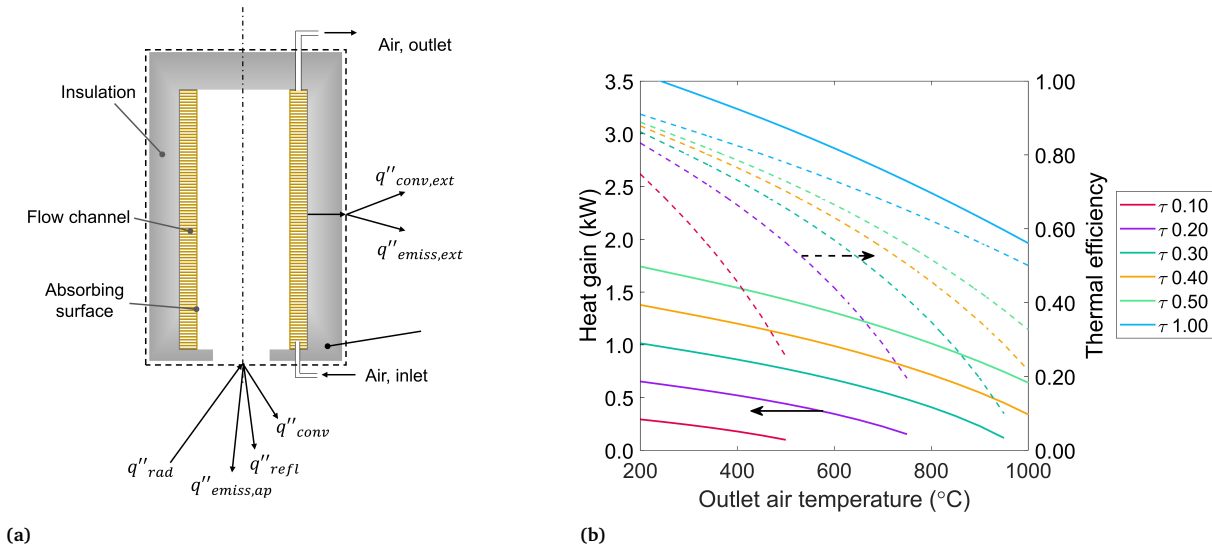

Fig. S7 (a) Solar air receiver, showing heat gains and losses modeled, and (b) results for various transmission values and temperatures, showing thermal efficiency (dashed, right axis), and heat gain (solid, left axis), for a DNI of 1000 W/m^2.

References

1 T. L. Bergman, Adrienne Lavine, Franck Incropera, and David Dewitt. *Introduction to heat transfer*. Wiley, Hoboken, NJ, 6th ed edition, 2011. OCLC: ocn739732416.

2 J.E. Braun and J.C. Mitchell. Solar geometry for fixed and tracking surfaces. *Solar Energy*, 31(5):439–444, 1983.

3 I. Hischier, P. Leumann, and A. Steinfeld. Experimental and Numerical Analyses of a Pressurized Air Receiver for Solar-Driven Gas Turbines. *Journal of Solar Energy Engineering*, 134(2):021003, May 2012.

4 Soteris A Kalogirou. Environmental Characteristics. page 76.

5 Sudesh Kumari, R. Turner White, Bijandra Kumar, and Joshua M. Spurgeon. Solar hydrogen production from seawater vapor electrolysis. *Energy & Environmental Science*, 9(5):1725–1733, 2016.

6 Michael J. Moran, editor. *Fundamentals of engineering thermodynamics*. Wiley, Hoboken, N.J, 8th ed edition, 2014. OCLC: ocn879865441.

7 Vikas R. Patil, Fabio Kiener, Adrian Grylka, and Aldo Steinfeld. Experimental testing of a solar air cavity-receiver with reticulated porous ceramic absorbers for thermal processing at above 1000 °C. *Solar Energy*, 214:72–85, January 2021.

8 Peter Poživil, Simon Ackermann, and Aldo Steinfeld. Numerical Heat Transfer Analysis of a 50 kWth Pressurized-Air Solar Receiver. *Journal of Solar Energy Engineering*, 137(6):064504, December 2015.

9 Jan Szargut. *Exergy Method: Technical and Ecological Applications*. 2005.

10 Huld T and Pinedo Pascua I. Typical Meteorological Year. 2017. Publisher: European Commission.